# Spatial Downscaling of MODIS Land Surface Temperature Based on Geographically Weighted Autoregressive Model

Shumin Wang ⬡, Xiaobo Luo ⬡, and Yidong Peng ⬡, *Student Member, IEEE*

*Abstract*—**Land surface temperature (LST) is a key parameter in numerous thermal environmental studies. Due to technical constraints, satellite thermal sensors are unable to supply thermal infrared images with simultaneous high spatial and temporal resolution. LST downscaling algorithms can alleviate this problem and improve the spatiotemporal resolution of LST data. Spatial nonstationary and spatial autocorrelation coexist in most spatial variables. The spatial characteristics of the LST should be fully considered as a spatial variable in the downscaling process. However, previous studies on LST downscaling considered only spatial nonstationary, and spatial autocorrelation was neglected. In this article, we propose a new algorithm based on the geographically weighted autoregressive (GWAR) model for LST spatial downscaling. The digital elevation model and normalized difference build-up index were chosen as explanatory variables to downscale the spatial resolution of the moderate resolution imaging spectroradiometer LST data from 1000 to 100 m, and Lanzhou and Beijing were taken as the study areas. The performance of the GWAR model was compared with that of the thermal data sharpening (TsHARP) model and the geographically weighted regression (GWR) model. The Landsat 8 LST was used to verify the downscaled LST. The results indicate that the GWAR-based algorithm outperforms the TsHARP- and GWR-based algorithms with lower root mean square error (Beijing: 1.37 °C, Lanzhou: 1.76 °C) and mean absolute error (Beijing: 0.86 °C, Lanzhou: 1.33 °C).**

*Index Terms*—**Geographically weighted autoregressive (GWAR), land surface temperature (LST), Landsat 8, moderate resolution imaging spectroradiometer (MODIS), spatial downscaling.**

## I. INTRODUCTION

LAND surface temperature (LST) is one of the key parameters that influences the environment and ecological systems

Shumin Wang is with the Institute of Computer Science and Technology, Chongqing University of Posts and Telecommunications, Chongqing 400065, China (e-mail: wangsm@foxmail.com).

Xiaobo Luo is with the Institute of Computer Science and Technology, Chongqing University of Posts and Telecommunications, Chongqing 400065, China, and also with the Chongqing Institute of Meteorological Sciences, Chongqing 401147, China (e-mail: luoxb@cqupt.edu.cn).

Yidong Peng is with the Chongqing Key Laboratory of Image Cognition, Chongqing University of Posts and Telecommunications, Chongqing 400065, China (e-mail: eadonlife@yahoo.com).

and is involved in many land surface processes [1]. LST is widely used in soil moisture studies [2], surface urban heat island and environment monitoring [3], [4], environmental biogeochemical process simulation [5], and climate change assessment [6]. In recent years, greater attention has been focused on the importance of LST.

It is difficult to obtain the spatial and temporal distributions of LST at regional and global scales using conventional ground observation. Thermal infrared remote sensing can detect and describe the spatial differences and diversities of LST dynamically and macroscopically [7]. Research study on the urban thermal environment requires LST data with high spatial and temporal resolutions. Because the spatial and temporal resolutions of the thermal infrared data are inconsistent, it is difficult to obtain data with both high spatiotemporal resolution, i.e., high temporal resolution is connected with low spatial resolution and vice versa. For example, the spatial resolutions of the Advance Spaceborne Thermal Emission and Reflection Radiometer, Thematic Mapper, Enhanced Thematic Mapper Plus, and Operational Land Imager (OLI) are much higher (30 m and 15 m), but their imaging frequency is much lower at 16 days [8]–[12]. Furthermore, the impact of clouds also reduces the probability of acquiring clear data. Other types of thermal infrared data with a lower spatial resolution and higher temporal resolution are available, such as moderate resolution imaging spectroradiometer (MODIS) and advanced very high-resolution radiometer. These satellite systems can image the entire earth every 1–2 days, but the spatial resolution is limited to 250 m [13]–[16]. To obtain high-resolution spatiotemporal data, it is necessary to process thermal infrared data using selected methods, and LST downscaling is one of these effective methods [17], [18]. LST downscaling combines the images obtained from the same or different sensors to obtain LST images with finer spatiotemporal resolution [16], [19].

Zhan *et al.* divided the disaggregated LST into two subbranches, including thermal sharpening and temperature unmixing. Among these, LST downscaling belongs to the thermal sharpening type [16]. According to the physical significances of keeping images or not, the downscaling models can be roughly divided into image fusion and relationship invariant models. The image fusion model fuses the high-resolution data with coarse- and medium-resolution thermal infrared data to obtain data with high resolution. Two types of fusion methods exist. One type of model is the linear model. In the linear model, the

reflectance of the high-resolution image is calculated from the linear model, which is generated in the low-resolution image to obtain a reflectance image with finer resolution [20]. Gao *et al.* [21] proposed a spatial and temporal adaptive reflectance fusion model (STARFM) for fusion of the MODIS and Landsat images with the assumption that the reflectance values of high- and low-resolution images do not change if the land cover types are not changed over time. Weng *et al.* [22] applied the STARFM model proposed by Gao *et al.* to the thermal infrared band and fused MODIS and Landsat data to obtain LST data with the same spatial resolution as Landsat. Mingquan *et al.* [23] proposed an improved spatial and temporal data fusion approach to generate the synthetic daily normalized difference vegetation index (NDVI) and validated the results of this method using the veritable MODIS NDVI time series. The second model is the unmixing model, which is based on the linear mixing theory. This model assumes that the mixed responses of each land cover type combine the reflectivity of each low-resolution spatial pixel to disaggregate the coarse resolution images via a linear mixed model [24], [25]. Zhukov *et al.* [26] used the moving window to find similar pixels and fused multisensor image data with different resolutions using the unmixing model. Maselli [27] used the Euclidean distance to calculate the weights of different coarse-resolution image pixels, subsequently estimated the average of the reflectivity of each land cover type in the entire image, and finally analyzed the obtained images.

Another proposed method obtains the spectral characteristics and physical meaning between the downscaled LST and the original LST. This method includes three types: spectral methods, modulation method, and statistical regression. The methods assume that there are many invariant spatial relationships in the process of downscaling [28]. Kustas *et al.* [29] proposed the DisTrad algorithm, which assumed that the relationship between LST and NDVI is scale invariant. To downscale LST, Agam *et al.* proposed the thermal data sharpening (TsHARP) algorithm, which is generated based on the DisTrad algorithm. The TsHARP method added different regression relationships to improve the downscaling results [30], [31]. Qiu *et al.* [32] proposed a refinement spectral index in the DisTrad model, which showed that the LST downscaling model is more robust by the performance of enhanced vegetation index for LST subpixel mapping. Pan *et al.* proposed a new model to downscale the LST, which used the normalized difference water index (NDWI), normalized difference sand index, and normalized difference build-up index (NDBI) to downscale the LST. The model can be further applied in middle-high and middle-low spatial resolutions [33]. To improve the downscaled performance, certain studies have considered nonlinear regression methods between LST and other explanatory variables. Bindhu *et al.* proposed the nonlinear disaggregated model (NL-DisTrad) and added an artificial neural network model to generate the residual at coarse resolution to downscale the LST and estimate evapotranspiration [34]. Hutengs and Vohland [35] and Yang *et al.* [36] used the random forest model to describe the relationship between the LST and explanatory variables to downscale the LST.

The above-mentioned methods are based on global characteristics. In recent years, selected scholars have studied the local characteristics between variables and began to consider the spatial nonstationary between the LST and auxiliary parameters [37], [38]. Zakšek and Oštir [4] used a moving window method to improve the spatial resolution of SEVIRI-LST data to 1000 m. Duan and Li introduced the geographically weighted regression (GWR) model into LST downscaling and compared it with the TsHARP-based global model. The results showed that the GWR model performed better than the traditional global model [39]. Pereira *et al.* [40] used ASTER thermal infrared data, multispectral data, and NDVI data to perform LST downscaling using the geographically weighted regression kriging (GWRK) method and achieved better downscaling results. Peng *et al.* used a method based on the geographically and temporally weighted regression (GTWR) model to downscale the MODIS LST data from 1000 to 100 m and compared it with the GWR model. The results of the GTWR-based algorithm were superior to those of the GWR-based algorithm [41]. The current local models for LST downscaling mainly consider the spatial nonstationary, whereas the spatial autocorrelation of LST is ignored.

Based on the abovementioned problems and with consideration of both spatial nonstationary and spatial autocorrelation, we proposed a new algorithm based on the geographically weighted autoregressive (GWAR) model for LST spatial downscaling. First, we analyzed the spatial autocorrelation of LST. Second, by comparing the results of the digital elevation model (DEM) and NDBI as the explanatory variables and the DEM and NDVI as the explanatory variables, we chose the DEM and NDBI as the explanatory variables and downscaled the MODIS LST spatial resolution from 1000 to 100 m. Finally, the downscaling results of the GWAR-based algorithm was compared with the downscaling results of the TsHARP and GWR-based algorithms, and the Landsat 8 LST to verify the downscaling LSTs.

## II. STUDY AREA AND DATASETS

### A. Study Area

This study selected two Chinese cities with different topographical features as the study areas. Fig. 1 shows the geographical location of two study areas and two false-color images of Landsat 8 images over the study areas.

Study area A belongs to the Beijing municipality of China. The longitude and latitude range from $116°0'18''$ to $116°41'14''$E and from $39°45'01''$ to $40°14'17''$N, respectively. The annual temperature, annual precipitation, and meaning elevation of this area are approximately 12 °C, 700 mm, and 80 m, respectively, in study area A. Area A is mainly characterized by an impervious surface, vegetation, water, and bare soil.

Study area B belongs to the Lanzhou city of Gansu Province, located in Northwest China. The study area covers 1500 km$^2$ with the latitude from $35°56'14''$ to $36°17'60''$N and the longitude from $103°32'56''$ to $103°59'18''$E. The annual average temperature is approximately 10 °C in this area, but the temperature of this area varies greatly between summer and winter. The average temperature of the coldest month is approximately $-7$ °C and that of the hottest month is approximately 30 °C. This area has a large fluctuation in elevation, from 1500 to 2800 m.

TABLE I
CHARACTERISTICS OF THE LANDSAT 8 AND MODIS DATA COLLECTED IN THIS STUDY

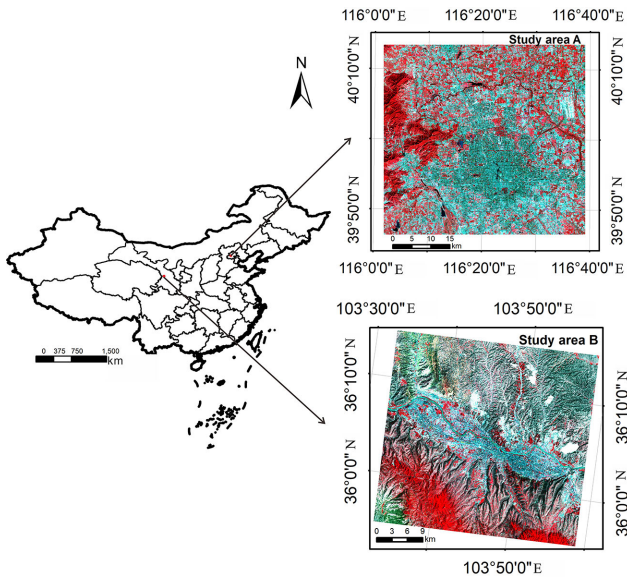| Area | Landsat 8 data | MODIS data |
|---|---|---|
| | Acquisition data/Time (UTC) | Acquisition data/Time (UTC) |
| Beijing | 09/12/2017 02:53:53 | 09/12/2017 02:25:00 |
| Lanzhou | 07/15/2016 03:44:22 | 07/15/2016 03:10:00 |



Fig. 1. Locations of the study areas with false-color images generated from Landsat 8 data (R: band 5, G: band 4, and B: band 3).

Area B is characterized by bare soil, water, vegetation, and an impervious surface.

### B. Datasets and Preparation

In this study, we chose the Shuttle Rader Topography Mission (SRTM) DEM images covering Lanzhou and Beijing. Table I shows the main characteristics of these images in the two study areas. As shown in Table I, there is approximately half an hour between the acquisition times of the MODIS and Landsat 8 images. Because of the short time difference, the solar geometries, orbital parameters, and the viewing (near-nadir) of the MODIS Terra platform are highly similar to those of the corresponding Landsat 8 [41].

*1) Landsat 8 Data:* Landsat 8 was launched by the National Aeronautics and Space Administration (NASA). Two sensors are carried by the Landsat 8 satellite, Thermal Infrared Sensor (TIRS) and OLI. The website of the Institute of Remote Sensing and Digital Earth Chinese Academy of Science[1] can download the Landsat 8 data. Preprocessing of downloaded Landsat 8 data is performed mainly by ENVI 5.1 software. First, radiometric calibration is used to convert the digital number of images to an absolute radiance value, with the aim of eliminating the error of the sensor itself. The next step is an atmospheric correction, a process that converts the radiance to actual surface reflectivity. Atmospheric correction eliminates the errors caused by the scattering, absorption, and reflection of the atmosphere. Finally, the images are cut to obtain the range of study. The Landsat 8 NDVI and NDBI are the explanatory variables for LST downscaling. The equations of NDVI and NDBI are written as follows:

$$\text{NDVI} = \frac{R_{\text{NIR}} - R_{\text{RED}}}{R_{\text{NIR}} + R_{\text{RED}}} \tag{1}$$

$$\text{NDBI} = \frac{R_{\text{SWIR1}} - R_{\text{NIR}}}{R_{\text{SWIR1}} + R_{\text{NIR}}} \tag{2}$$

where $R_{\text{NIR}}$, $R_{\text{RED}}$, and $R_{\text{SWIR1}}$ are the reflectance values of the near-infrared band, red band, and the first shortwave infrared band, respectively, and these bands correspond to Band 5, Band 4, and Band 6 of Landsat 8, respectively.

In this article, the Landsat 8 LST was used to verify the downscaled LSTs. Many methods are used to retrieve the LST from the satellite thermal infrared images. Due to the uncertainty of the Landsat 8 TIRS Band 11, the TIRS band 10 is used to estimate the LST through calibration notices published by the United States Geological Surface [42]. Therefore, we used the Landsat 8 Band 10 to retrieve the LST via the monowindow algorithm. Qin *et al.* [43] proposed the monowindow algorithm for retrieval of the LST with one thermal band. The monowindow algorithm is shown in the following equation: (3) shown at the bottom of this page, where $T_s$, $T_{10}$, and $T_a$ represent the LST, the brightness temperature of Landsat 8 TIRS Band 10, and the effective mean atmospheric temperature, respectively; and $a_{10}$ and $b_{10}$ are the constants, and their values for the Landsat 8 TIRS Band 10 are given in Table II [43]. The values of $C_{10}$ and $D_{10}$

[1][Online]. Available: http://www.gscloud.cn

$$T_S = \frac{a_{10}\left(1 - C_{10} - D_{10}\right) + \left[b_{10}\left(1 - C_{10} - D_{10}\right) + C_{10} + D_{10}\right]T_{10} - D_{10}T_a}{C_{10}} \tag{3}$$

TABLE II
DETERMINATION OF COEFFICIENTS $a_{10}$ AND $b_{10}$[46]

| Temperature Range | $a_{10}$ | $b_{10}$ | $R^2$ |
|---|---|---|---|
| 20 - 70°C | -70.1775 | 0.4581 | 0.9997 |
| 0 - 50°C | -62.7182 | 0.4339 | 0.9996 |
| -20 - 30°C | -55.4276 | 0.4086 | 0.9996 |

can be calculated by the following equations:

$$C_{10} = \varepsilon_{10}\,\tau_{10} \tag{4}$$

$$D_{10} = (1 - \tau_{10})\,[1 + (1 - \varepsilon_{10})\,\tau_{10}] \tag{5}$$

where $\varepsilon_{10}$ and $\tau_{10}$ represent the land surface emissivity and atmospheric transmittance, respectively. Three critical parameters are used to retrieve LST through the monowindow algorithm: the effective mean atmospheric temperature, land surface emissivity, and atmospheric transmittance [44], [45]. Among these, the effective mean atmospheric temperature is commonly used to estimate the upwelling atmospheric radiance. The near-surface temperature is obtained based on 15 local meteorological stations. The near-surface temperature is used to obtain the effective mean atmospheric temperature using a linear equation [46]. Two steps are applied to estimate the land surface emissivity. The first step uses the land cover map to distinguish different land cover types with a spatial resolution of 30 m. The second step uses the NDVI threshold method to estimate land surface emissivity [47]. The atmospheric transmittance is obtained from many factors, such as water vapor, aerosol, wavelength, and ozone. Among these, the atmospheric is the most important factor in determining the atmospheric transmittance and the derivation of atmospheric transmittance for Landsat 8 TIRS band in [46, Table 5].

When the error of the water vapor content and land surface emissivity is moderate, the accuracy level of the monowindow algorithm is approximately 1.4 K [42]. The mean error between the MODIS LST and *in situ* measured LST and Landsat 8 LST retrieved by the monowindow algorithm is approximately 1.6 K [48]–[50].

*2) MODIS LST Data:* The MODIS LST product (MOD11_L2, 1 km, collection 6) can be downloaded from the Reverb website.[2] The MODIS images must be registered to a UTM WGS 1984 reference system by the MODIS Reprojection Tool and georeferenced. The spatial resolution of the MOD11_L2 product is 1000 m. The LST was retrieved by the split-window algorithm, and the error is approximately 1 K [51]–[53]. The MODIS LST product with 1000 m spatial resolution was used as the auxiliary data for LST downscaling in this study.

*3) DEM Data:* The SRTM is an international project spearheaded by the National Geospatial Intelligence Agency and the NASA. The SRTM can supply DEM from 56 S to 60 N with finer resolution. In this study, the DEM images were downloaded

from the website[3] with 90-m spatial resolution. The DEM data with spatial resolutions of 100 and 1000 m are the explanatory variables used to downscale the LST in this study.

## III. METHODOLOGY

### A. Describing the GWAR Model

The GWR model extends the traditional regression model and is effective in describing the local regression relationship. The GWR model can estimate local parameters rather than global parameters in the regressive relationships [54] and can describe the nonstationary relationship between the explanatory variables and the explained variables by estimating the local regression coefficients.

A potential interdependence can occur between certain spatial variables in the same distribution area, which is known as spatial autocorrelation. The spatial autoregressive (SAR) model adds the independent variable $\bar{W}Y$ into a linear regression relationship, and this variable is used to explain the spatial autocorrelation [55].

Spatial nonstationary and spatial autocorrelation are always related in the context of modeling, and thus we could combine these two features into a mixed model. [56]. The GWAR model combines the GWR model with the SAR model. By adding the spatial autocorrelation into the GWR-based model, the combined model can reduce unstable estimates. The GWAR model can be expressed as follows [57]:

$$y_i = \beta_0(u_i, v_i) + \sum_{k=1}^{p} \beta_k(u_i, v_i)x_{ik} + \rho(u_i, v_i)\bar{W}_iY + \varepsilon_i \tag{6}$$

where $(u_i, v_i)$ denotes the coordinates of point $i$ in space; $y_i$ and $x_{ik}$ are the explained variable and the $k$th explanatory variable at point $i$, respectively; $\beta_0(u_i, v_i)$ is the intercept, and $\beta_k(u_i, v_i)$ is the local coefficients estimated of the independent $x_{ik}$ at point $i$; $\rho(u_i, v_i)$ is a autoregressive parameter to be estimated at point $i$; $\bar{W}_i$ is a spatial adjacency matrix that contains nonnegative elements of neighboring properties whose diagonal elements are zeros to prevent each observation from predicting itself; the parameter $\rho(u_i, v_i)$ represents different geographical locations and affects the $Y$-variable in the spatial diffusion process; $Y$ is the spatial sample of observations; and $\varepsilon_i$ is the regression residual at point $i$.

The parameters $\beta_0$ and $\beta_k$ in (6) are calculated as follows:

$$\hat{\beta}(u_i, v_i) = (X^T W(u_i, v_i)X)^{-1} X^T W(u_i, v_i)Y \tag{7}$$

where $\hat{\beta}(u_i, v_i)$ is the unbiased estimate of the regression coefficient $\beta$; $X$ and $Y$ represent the vectors for the explanatory and explained variables, respectively; and $W(u_i, v_i)$ is the weighting matrix used to ensure that observations near the specific point have larger weighted values. Four different kernel functions can estimate the $W(u_i, v_i)$. In this article, we selected the Gaussian function to calculate the weights, and thus $W(u_i, v_i)$ can be obtained as follows:

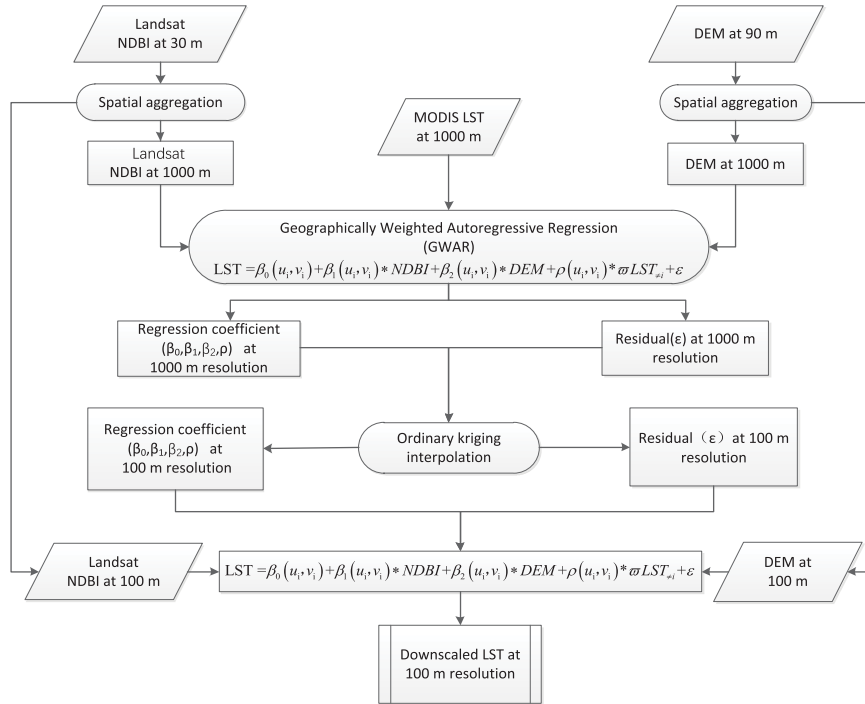$$W_{ij} = \exp\left(-\frac{d_{ij}{}^2}{b^2}\right) \tag{8}$$

Fig. 2. Schematic of the GWAR-based LST downscaling algorithm.

where $d_{ij}$ is the Euclidean distance between the points $i$ and $j$, and $b$ is the adaptive kernel bandwidth. The cross-validation method of local regression analysis is used to calculate the bandwidth [57]. The formula of this method is written as follows:

$$\mathrm{CV} = \frac{1}{n} \sum_{i=1}^{n} \left[ y_i - \hat{y}_{\neq i}(b) \right]^2 \qquad (9)$$

where the $\bar{y}_{\neq i}(b)$ represents the predicted value of $y_i$ from the GWAR model.

### B. GWAR-Based LST Downscaling Algorithm

It is important to choose the appropriate explanatory variables in the downscaling process. Many factors should be involved in the modeling process, including solid moisture, solar radiation, and land cover. [58]. Nevertheless, the selection of all of these parameters is difficult and unrealistic. In previous research studies, scholars focused greater attention on the relationship between NDVI and LST. However, due to the complex relationship between the LST and NDVI, the downscaled results are poor with a wide range of soil moisture [59].

DEM and NDBI were chosen as the explanatory variables in this article. The NDBI represents the built-up area, which is an important land cover type. The NDBI can describe the urban spatial extent and intensity of development and is an indicator of the urban impervious surface [60]. Elevation is recognized as a crucial factor in characterizing the variations of LST. The longitude and latitude reflect the influence of moisture on LST from different areas and the difference in solar radiation, respectively. In other words, the longitude and latitude are related to the LST [39]. Because these two parameters were input into the GWAR model, the parameters were not selected as explanatory variables.

Fig. 2 shows the schematic of the GWAR-based LST downscaling algorithm. We summarized the specific steps as follows:

1) The DEM and NDBI were aggregated to 1000 and 100 m. DEM and NDBI with a spatial resolution of 1000 m represent the MODIS LST pixel resolution, and DEM and NDBI with a spatial resolution of 100 m represent the explanatory variables at the Landsat 8 LST pixel resolution.

2) We use the GWAR model to establish a regression relationship between the MODIS LST, NDBI, DEM images, and the SAR variables at a spatial resolution of 1000 m, which can be expressed as follows:

$$
\begin{aligned}
\mathrm{LST}_i^{1000} =\ & \beta_0^{1000}(u_i, v_i) + \beta_1^{1000}(u_i, v_i)\, \mathrm{NDBI}_i^{1000} \\
& + \beta_2^{1000}(u_i, v_i)\, \mathrm{DEM}_i^{1000} \\
& + \rho^{1000}(u_i, v_i)\, \varpi\mathrm{LST}_{\neq i}^{1000} + \varepsilon_i^{1000}. \quad (10)
\end{aligned}
$$

In formula (10), $\mathrm{LST}_i^{1000}$ denotes MODIS LST at point $i$ with a spatial resolution of 1000 m; $\mathrm{NDBI}_i^{1000}$ is the aggregated Landsat 8 NDBI; $\mathrm{DEM}_i^{1000}$ is the aggregated DEM at the point $i$ with a spatial resolution of 1000 m; $\bar{\omega}\mathrm{LST}_{\neq i}^{1000}$ denotes the autoregressive variable and represents the LST of the surrounding observations that affect point $i$; $\beta_0^{1000}(u_i, v_i)$, $\beta_1^{1000}(u_i, v_i)$, $\beta_2^{1000}(u_i, v_i)$, $\rho^{1000}(u_i, v_i)$, and $\varepsilon_i^{1000}$ are the intercept, local coefficients, autoregressive coefficient, and residual of the regression location $i$ at a spatial resolution of 1000 m at point $i$, respectively; and $\mathrm{LST}_{\neq i}^{1000}$ is the influence of the surrounding observation points not including the point $i$.
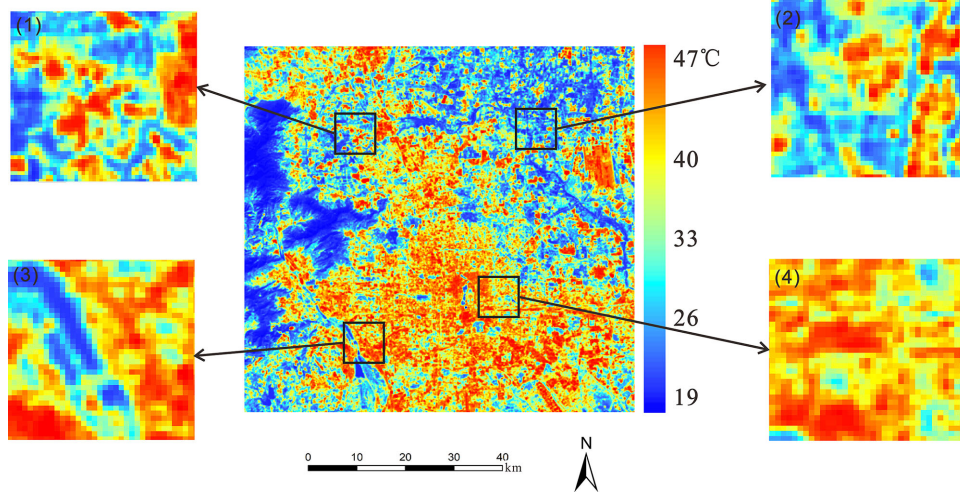
Fig. 3. Distribution of LST in Beijing.

1) Duan and Li [39] proposed that the ordinary kriging interpolation method is more suitable for improving the accuracy of LST downscaling than the simple spline tension interpolation method. Therefore, the ordinary kriging interpolation method is used in this article to interpolate the spatial resolution of the residual and variables from 1000 to 100 m.

2) Kustas et al. [29] indicated that certain relationships exist between NDVI and LST, and these relationships are invariable in different spatial resolutions. Zhan [16] indicated that the relationship established at the lower spatial resolution could be directly used at a higher resolution. Many studies showed that the relationship between LST and the explanatory variables is independent with spatial resolution [28], [30], [58], [59]. In this article, we assumed that the relationship between LST and the independent variables with a spatial resolution of 1000 m is scale-invariant, and based on this assumption, the relationship between LST with DEM, NDBI, and autoregressive variable in a 100-m spatial resolution can be written as follows:

$$
\begin{aligned}
\mathrm{LST}_i^{100} = {} & \beta_0^{100}\left(u_i, v_i\right) + \beta_1^{100}\left(u_i, v_i\right) \mathrm{NDBI}_i^{100} \\
& + \beta_2^{100}\left(u_i, v_i\right) \mathrm{DEM}_i^{100} \\
& + \rho^{100}\left(u_i, v_i\right) \varpi \mathrm{LST}_{\neq i}^{100} + \varepsilon_i^{100}
\end{aligned}
\tag{11}
$$

where $\mathrm{LST}_i^{100}$ is the downscaled LST with a spatial resolution of 100 m at point $i$, and $\mathrm{LST}_{\neq i}^{100}$ represents that the LST of point $i$ is not included in the autoregressive variables.

We use the TsHARP- and GWR-based algorithms to compare with the abovementioned GWAR-based algorithm. In this study, we used the coefficient of determination ($R^2$), root mean square error (RMSE) and mean absolute error (MAE) to verify the downscaled results. Higher $R^2$ and lower RMSE and MAE represent better downscaled results.

## IV. RESULTS AND DISCUSSION

### A. Spatial Autocorrelation Analysis of LST

The spatial autocorrelation is defined as potential interdependence between the spatial variables in the spatial distribution area, i.e., the value of the spatial variable is always connected to the values of the same variable at the adjacent location. Spatial autocorrelation is caused by intrinsic relevancy between the spatial variables.

Fig. 3 presents the distribution of LST in Beijing. To observe the details of the spatial distribution, (1)–(4) in Fig. 3 indicate four enlarged portions of the LST image. Additionally, (1)–(4) display a strong spatial dependence and pixels with similar LST cluster together. Higher LST (red spots) is surrounded by high LST (orange spots), and similarly, lower LST (blue spots) is surrounded by low LST (light blue spots). High temperature (red spots) is connected to low temperature (blue spots) by the middle temperature (yellow spots). The LST distribution of Lanzhou has the same distribution as that of Beijing.

Moran's $I$ is an index that is always used to analyze spatial autocorrelation. Moran's $I$ measures the relationship between the adjacent spatial attributes. Values of Moran's $I$ range from $-1$ to 1. Moran's $I$ greater than 0 indicates positive spatial correlation, and the larger the value, the more obvious the spatial autocorrelation. In contrast, Moran's $I$ less than 0 indicates negative spatial correlation, and the smaller the value, the greater the spatial difference. If Moran's $I$ is equal to 0, the data present a random distribution. Moran's $I$ is defined as follows:

$$
\text{Moran's } I = \frac{n}{\sum\sum W_{ij}} \frac{\sum\sum W_{ij}\left(X_i - \overline{X}\right)\left(X_j - \overline{X}\right)}{\sum\left(X_i - \overline{X}\right)^2}
\tag{12}
$$

where $n$ is the number of total elements, and $X_i$ denotes observation of the variable at point $i$, $\overline{X}$ denotes the average of variable $X$, and $W_{ij}$ is the spatial weight function, which represents the position relationship between the observed values [55].

| Parameter | Beijing | Lanzhou |
|---|---|---|
| Moran's I | 0.71 | 0.97 |
| Z-score (°C) | 35.75 | 59.88 |
| P-value | 0.00 | 0.00 |

Two important indicators in spatial statistics are the *p*-value and *z*-score. The *p*-value represents the probability that the spatial variable is caused by a random process, and the expression of the *p*-value is different according to different distributions of data. Usually, if the *p*-value is less than 0.05, it indicates that the data were not generated randomly and that the data have important research significance. The *z*-score represents a multiple of the standard deviation, and it can reflect the dispersion and clustering of the data. The *z*-score can be a positive or a negative value. The equation of the *z*-score is given as follows:

$$Z = \frac{x - \mu}{\sigma} \tag{13}$$

where $x$ and $\mu$ are the primitive value and the average value, respectively, and $\sigma$ is the standard deviation. In general, a *z*-score greater than $+2.5$ indicates that the dataset is clustered, whereas a *z*-score that is less than $-2.5$ indicates that the dataset is dispersed.

In Table III, the *p*-values of these two areas are 0.00, which proves that these two datasets are impossible to be generated randomly. The *z*-scores are 35.75 °C (Beijing) and 59.88 °C (Lanzhou), which show that the datasets are highly spatially clustered. The Moran's *I* values are 0.71 (Beijing) and 0.97 (Lanzhou), indicating that the LST has a strong positive spatial autocorrelation and is highly clustered in the study areas.

In terms of spatial variables, spatial nonstationary and spatial autocorrelation of LST coexist. Therefore, we should not only examine the spatial nonstationary of LST but also focus attention on the spatial autocorrelation in the process of LST downscaling.

### B. Regression Analysis and Selection of Explanatory Variables

The TsHARP is a traditional LST downscaling algorithm. The GWR-based algorithm is a local model for spatial downscaling that improves the spatial resolution of the LST data and has better downscaled results than the traditional TsHARP algorithm [39]. The GWAR-based downscaling algorithm adds spatial autocorrelation to the GWR model and is mainly compared with the GWR-based algorithm.

Fig. 4 shows the $R^2$ of the GWR and GWAR models at a 1000-m spatial resolution. The GWR and GWAR models using the DEM and NDBI as the explanatory variables are denoted as GWR_BD and GWAR_BD, respectively, and these two models using the DEM and NDVI as explanatory variables are denoted by GWR_VD and GWAR_VD, respectively. First, the $R^2$ values of the GWAR_BD and GWR_BD model are 0.96 and 0.91 in Beijing and 0.92 and 0.84 in Lanzhou, respectively. The $R^2$ values of the GWAR_VD and GWR_VD models are 0.92 and
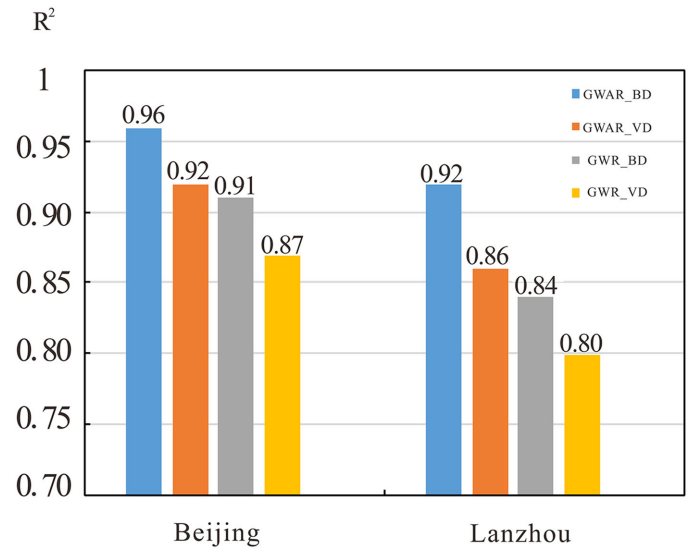


Fig. 4. Coefficient of determination ($R^2$) of the regression models with a spatial resolution of 1000 m.

0.87 in Beijing and 0.86 and 0.80 in Lanzhou, respectively. When the explanatory variables are the same (DEM and NDBI or DEM and NDVI), the regression results of the GWAR model are better than those of the GWR model at coarse resolution. Second, the $R^2$ values of GWAR_BD and the GWAR_VD are 0.96 and 0.92 in Beijing and 0.92 and 0.86 in Lanzhou, respectively. In these two areas, the $R^2$ of the variable combination of DEM and NDBI is significantly increased compared with the variable combination of DEM and NDVI using the same model.

Habin *et al.* compared the NDVI and NDBI as an index to research the surface urban heat island. The results indicated that with changing of the season, the linear relationship between LST and NDBI is stronger than the relationship between LST and NDVI [61]. Govil *et al.* [62] proved that the NDBI is better suited to downscaling LST than the normalized multiband drought index (NMDI), NDVI, and NDWI in almost every season. The relationship between the LST and NDVI is nonlinear and is strongly affected by season, whereas the relationship between LST and NDBI shows a linear pattern in every season. When the season changes, the relationship between LST and NDBI is more stable than the NDVI.

Fig. 5 shows the Landsat 8 NDVI and NDBI with MODIS LST at a spatial resolution of 1000 m in Lanzhou. As shown in Fig. 5(a), when the NDVI is greater than 0, the relationship between the LST and NDVI is negative and linear. However, the relationship of LST and NDVI shows a triangular relationship in the entire study area. Comparing Fig. 5(a) and (b), the Landsat NDBI is more connected with the MODIS LST with higher $R^2$ (0.70) than Landsat NDVI ($R^2$: 0.47). Normally, the LST and the water surface have no linear relationship with NDVI, and therefore, the water areas have a higher error [63]

Therefore, we conclude that first, the relationship between NDBI and LST has a more stable linear correlation than the NDVI and LST when the time and season change, and second, the relationship between NDVI and LST is not a linear
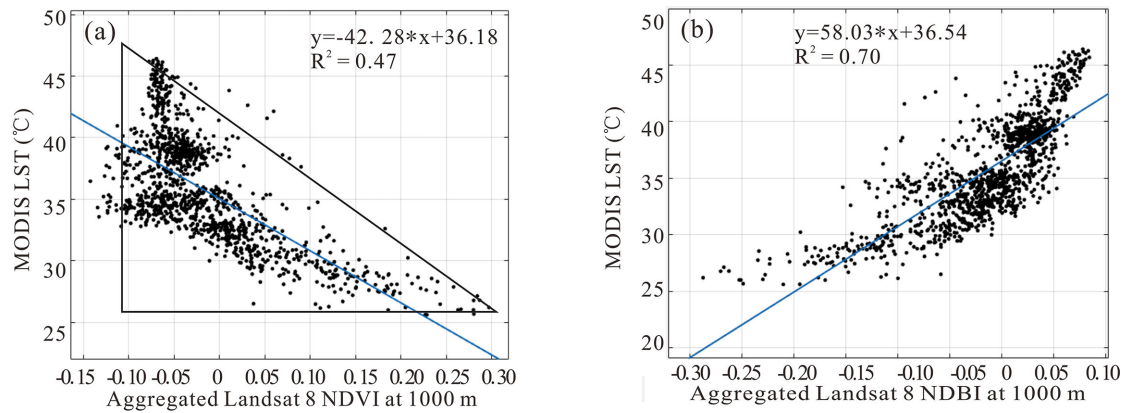
Fig. 5. Scatterplots and regression relationship between (a) Landsat NDVI and (b) Landsat NDBI with MODIS LST at a 1000-m spatial resolution.
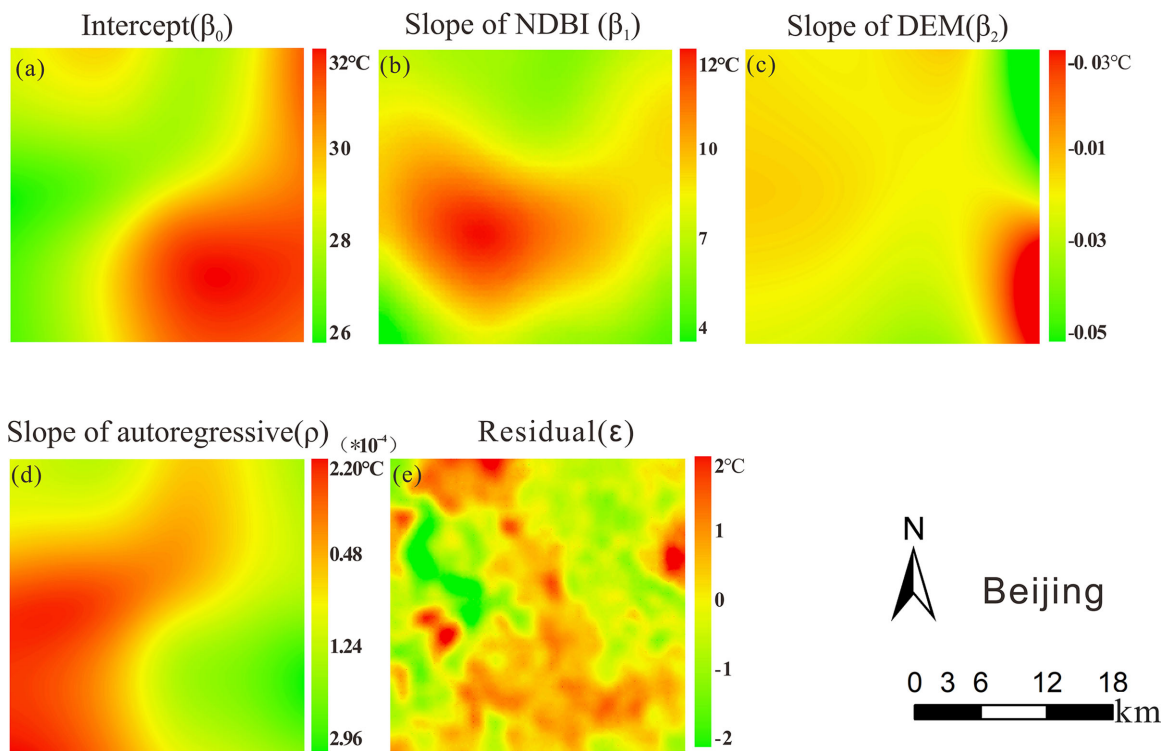


Fig. 6. Spatial distribution of the kriging-interpolated regression coefficients and residual for the GWAR-based algorithm in Beijing. (a) Intercept ($\beta_0$). (b) Slope of NDBI ($\beta_1$). (c) Slope of DEM ($\beta_2$). (d) Slope of autoregressive ($\rho$). (e) Residual ($\varepsilon$).

relationship in the high soil water content, bare soil, and other land cover types. In analyzing the above-mentioned points, the GWAR-based algorithm using the DEM and NDBI as the explanatory variables is more suitable for describing the MODIS LST distribution in the study areas.

Local parameters offer an effective method for analyzing the spatial relationship between the explained variable and explanatory variables. Figs. 6 and 7 show the spatial patterns of the kriging-interpolated regression coefficients and residual for the GWAR-based algorithm (the explanatory variables are DEM and NDBI) in Beijing and Lanzhou. The spatial heterogeneity is shown by the spatial distribution of the parameters.

In Figs. 6(a) and 7(a), the slope of the intercept ranges are 26–32 °C and 41–54 °C in Beijing and Lanzhou, respectively. In

Fig. 6(b), the slope of NDBI is 4–12 °C. The value in the middle of the study area is larger than at the edge, and thus the influence of NDBI is higher in the middle than at the edge in Beijing. This may be related to the large number of building in the middle of Beijing. Because the terrain is relatively flat in Beijing, the slope of the DEM has a small fluctuation. However, the slope of the autoregressive [see Fig. 6(d)] has a larger range and an uneven regional distribution. In the southwest, the autoregressive is positive, but it is negative in the southeast. The result indicates that the spatial autocorrelation is uneven in different regions, which might be caused by the different land cover types.

In Lanzhou (see Fig. 7), the images are relatively smoother. The slope of NDBI has a large range of 33–57 °C, and that in the northeast is larger than in the southwest. The slope of the DEM
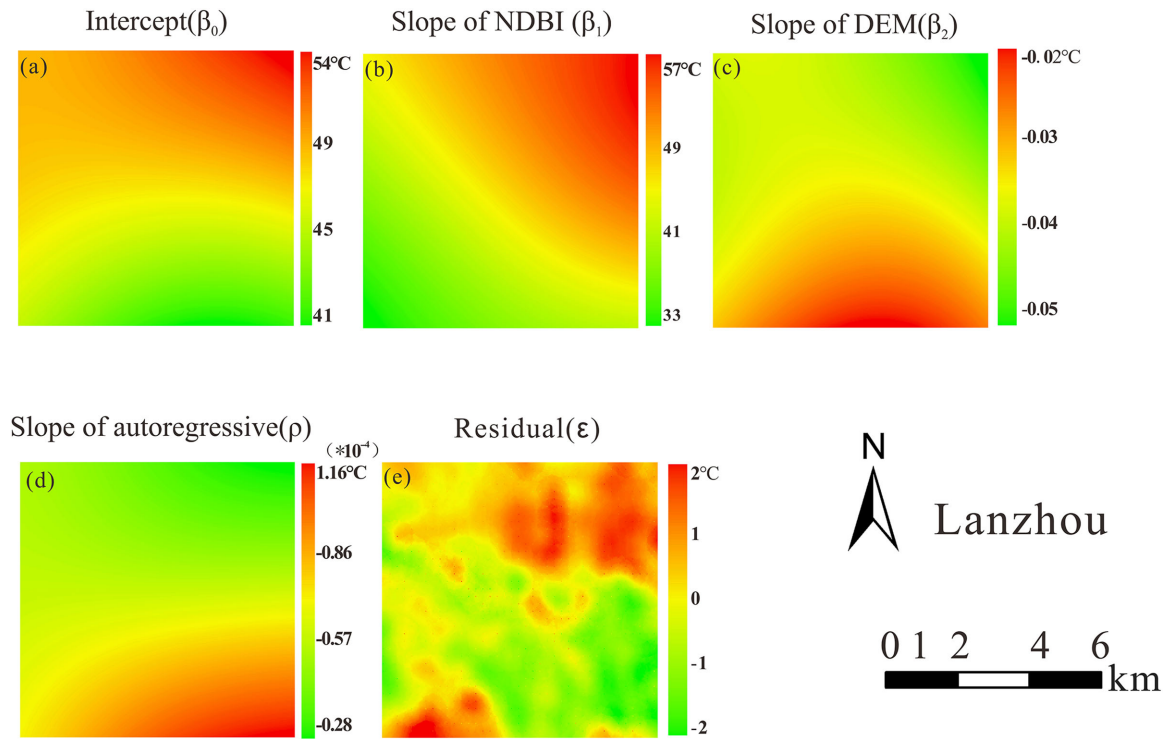
Fig. 7. Spatial distribution of the kriging-interpolated regression coefficients and residual for the GWAR-based algorithm in Lanzhou. (a) Intercept ($\beta_0$). (b) Slope of NDBI ($\beta_1$). (c) Slope of DEM ($\beta_2$). (d) Slope of autoregressive ($\rho$). (e) Residual ($\varepsilon$).

TABLE IV
STATISTICS OF KRIGING-INTERPOLATED REGRESSION COEFFICIENTS AND RESIDUAL FOR THE GWAR MODEL

| Parameter | Beijing | | | Lanzhou | | |
|---|---|---|---|---|---|---|
| | Min | Max | Mean | Min | Max | Mean |
| $\beta_0$ (℃) | 26 | 32 | 29 | 41 | 54 | 47.5 |
| $\beta_1$ (℃) | 4 | 12 | 8 | 33 | 57 | 45 |
| $\beta_2$ (℃) | -0.05 | 0.02 | -0.015 | -0.005 | -0.002 | -0.0015 |
| $\rho$ (℃) | -0.000296 | 0.00022 | -0.000038 | -0.000206 | -0.0000277 | -0.000116 |
| $\varepsilon$ (℃) | -1.75 | 1.98 | 0.115 | -2.01 | 1.19 | -0.41 |

also has an uneven distribution, and that of the north is obviously larger than that of the south. The slope of the autoregressive shows the same phenomenon in that the different regions have an uneven distribution. In these two areas, the distribution of the residual [see Figs. 6(e) and 7(e)] is uneven, but both of the residuals range from −2 to 2 °C. The spatial distributions of these kriging-interpolated regression coefficients and residuals are uneven, showing that study of the spatial characteristics is important.

Table IV summarizes the min, max, and mean of the parameters presented in Figs. 6 and 7. Observing and analyzing the

values of these variables indicate that the relationship between DEM and Landsat 8 NDVI with MODIS LST shows spatial heterogeneity and spatial autocorrelation. Therefore, it is necessary to consider both spatial nonstationary and spatial autocorrelation in the process of LST downscaling.

### C. Analysis of the Downscaled Results

*1) Analysis of the Relationship Between Landsat 8 LST and MODIS LST:* The Wan refinements and validation of the collection-6 MODIS LST indicated that the collection-6

TABLE V
LINEAR RELATIONSHIP BETWEEN MODIS LST AND LANDSAT 8 LST AT A
1000-M SPATIAL RESOLUTION, MODEL: $\text{LST}_{\text{MODIS}} = a* \text{LST}_{\text{Landsat}} + b$

|  | **Beijing** | **Lanzhou** |
|---|---|---|
| **$R^2$** | 0.92 | 0.90 |
| **a (°C)** | 0.85 | 0.81 |
| **b (°C)** | 3.50 | 4.20 |
| **RMSE(°C)** | 1.82 | 1.97 |

products are much better than the collection-5 products and that the mean error is less than 1 K in most sites [64]. A large quantity of research studies have indicated that if no ground observation data are available, then the accuracy of the MODIS LST product inversion can be used to validate the accuracy of LST [65]–[67]. In this article, we used the collection-6 MODIS LST to analyze the relationship between MODIS LST and Landsat LST. Table V shows the linear relationship between MODIS LST and Landsat 8 LST at a 1000-m spatial resolution with a model: $\text{LST}_{\text{MODIS}} = a* \text{LST}_{\text{Landsat}} + b$.

In these two datasets, the Landsat 8 LST generally agrees with the MODIS LST at a 1000-m spatial resolution. In both of these study areas, the $R^2$ reaches 0.90 and the RMSEs are less than 2 °C (1.82 and 1.97 °C). Duan and Li [39] used the ASTER LST product as reference LST data to evaluate the performance of the GWR-based LST downscaling algorithm and reported that the RMSE between ASTER LST and MODIS LST is approximately 2.1 K. The RMSE between Landsat 8 LST and the MODIS LST at a 1000-m spatial resolution is lower than that of the MODIS LST and ASTER LST. Hutengs and Vohland [35] indicated that the RMSE between Landsat 8 LST and MODIS LST is approximately 1.2 °C and is higher than the RMSE between MODIS LST and Landsat 7 LST. Peng *et al.* [41] used the Landsat 8 retrieved LST as the reference LST to compare the results of different algorithms. Therefore, the accuracy of Landsat 8 LST could be used to verify the downscaled LSTs. In this article, we used the Landsat 8 retrieved LST as the reference to verify the downscaled LSTs.

*2) Evaluating the Accuracy of Downscaled LST Data:* In this study, the combinations of DEM and NDBI and DEM and NDVI were used as the explanatory variables for the experiment. We compared the GWAR-based algorithm with the traditional global TsHARP- and local GWR-based algorithms. Figs. 8 and 9 show the MODIS LST, Landsat 8 LST, and the downscaled LSTs of all algorithms. Figs. 8(a) and 9(a) show the MODIS LST at a 1000-m spatial resolution in Beijing and Lanzhou, respectively. As shown in MODIS LST at a 1000-m spatial resolution [see Figs. 8(a) and 9(a)], the demarcation of the land cover types is blurred, and selected types cannot be judged accurately. Figs. 8(b) and 9(b) present the Landsat 8 LST at a 100-m spatial resolution. Figs. 8(c) and 9(c) show the down-scaled LST of the TsHARP algorithm at a 100-m spatial resolution. GWAR_VD and GWR_VD denote the DEM and NDVI

as the explanatory variables for LST downscaling. Similarly, GWAR_BD and GWR_BD denote the DEM and NDBI as the explanatory variables for LST downscaling. Figs. 8(d)–(g) and 9(d)–(g) show the downscaled LSTs at a 100-m spatial resolution of the GWR_VD-based, GWAR_VD-based, GWR_BD-based, and GWAR_BD-based algorithms from these two study areas, respectively.

Comparing the LST images, the spatial distribution of the downscaled LSTs is consistent with the Landsat 8 LST. The results of TsHARP algorithm [see Fig. 8(c) and 9(c)] contain a boxy artifact in both areas. This phenomenon is caused by the LST variability in soil moisture in the coarse resolution images, but the LST downscaling process of the TsHARP algorithm does not consider this problem [68]. The downscaled LSTs of the GWR_VD- and GWR_BD-based algorithms [see Figs. 8(d) and (f) and 9(d) and (f)] have a smoothing effect. Two possible reasons can explain this phenomenon. A common problem exists in the regression process that is based on the minimum mean square error, which underestimates the high values and overestimates the low values, and in the process of spatial aggregation, the NDBI, NDVI, and DEM from 100 m or 90 m to 1000 m are replaced by the average of the surrounding pixel, which causes loss of the detailed information in NDBI, NDVI, and DEM, as also reported by in related studies [39], [41], [69]. For the algorithm with the same explanatory variables [see Fig. 8(d)–(g)], the downscaling LST results of the GWAR-based algorithm showed more spatial details than the GWR-based algorithm. Fig. 9(e) and (g) used the GWAR-based algorithm; Fig. 9(e) used the DEM and NDVI as the explanatory variables, whereas Fig. 9(g) used the DEM and NDBI as the explanatory variables. Comparing these two images, Fig. 9(e) shows that the areas with rivers and lakes, etc., are not well reconstructed, but Fig. 9(g) is closer to the Landsat 8 LST. The reason for this observation is that the GWAR_VD-based algorithm cannot capture the triangular relationship between NDVI and LST in the soil moisture and areas with a wide range of vegetation. Because autocorrelation is considered and the DEM and NDBI are used as the explanatory variables, the smoothing effect of the GWAR-based algorithm is alleviated, and the downscaled results are better in the full soil moisture content. Therefore, the GWAR algorithm with the explanatory variable combination of DEM and NDBI reflects more spatial details and has better downscaled results than the other algorithms.

The RMSE and MAE values between the downscaled LSTs and Landsat 8 LST of Beijing and Lanzhou are shown in Table VI and Table VII, respectively. The RMSE and MAE can be calculated as follows:

$$\text{RMSE} = \sqrt{\frac{1}{n} \sum\nolimits_{i=1}^{n} \left(\text{LST}_S - \text{LST}_R\right)^2} \quad (14)$$

$$\text{MAE} = \frac{1}{n} \sum_{i=1}^{n} |\text{LST}_S - \text{LST}_R| \quad (15)$$

where $n$ represents the amount of pixels, and $\text{LST}_S$ and $\text{LST}_R$ are the downscaled LST and the reference LST (Landsat 8 LST), respectively.
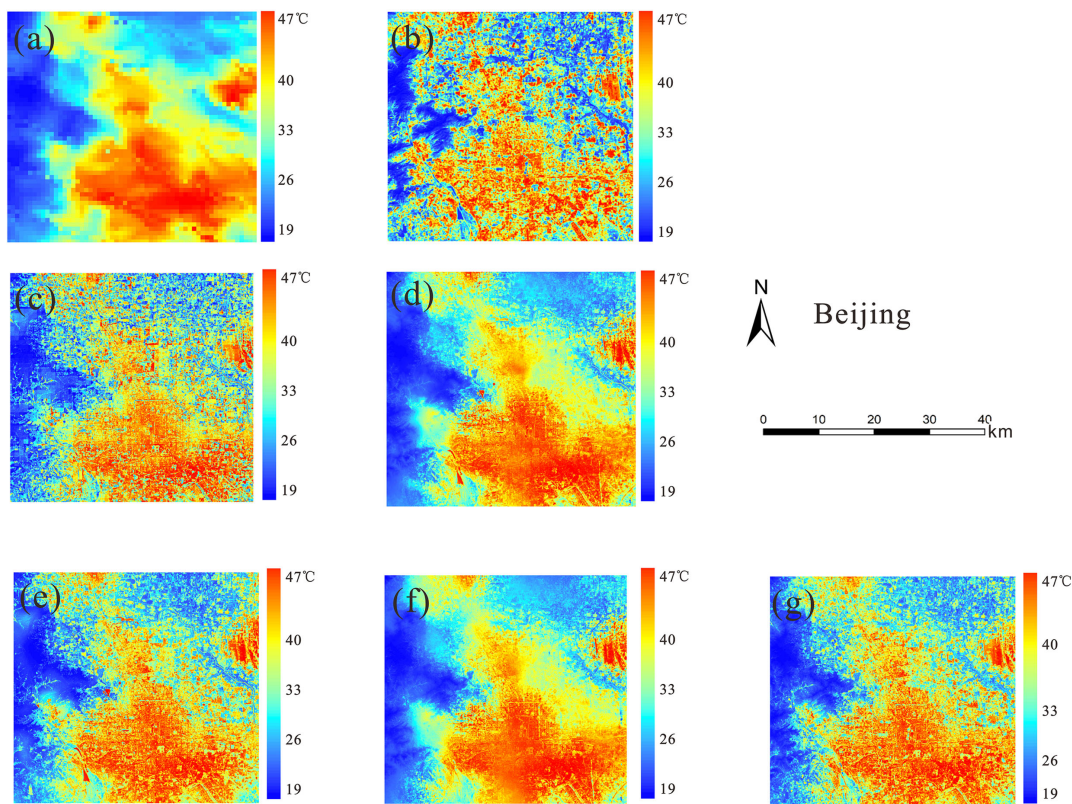
Fig. 8. Spatial distribution of LSTs in Beijing. (a) MODIS LST (1000 m). (b) Landsat 8 LST (100 m). (c) TsHARP downscaled LST (100 m). (d) GWR_VD downscaled LST (100 m). (e) GWAR_VD downscaled LST (100 m). (f) GWR_BD downscaled LST (100 m). (g) GWAR_BD downscaled LST (100 m).
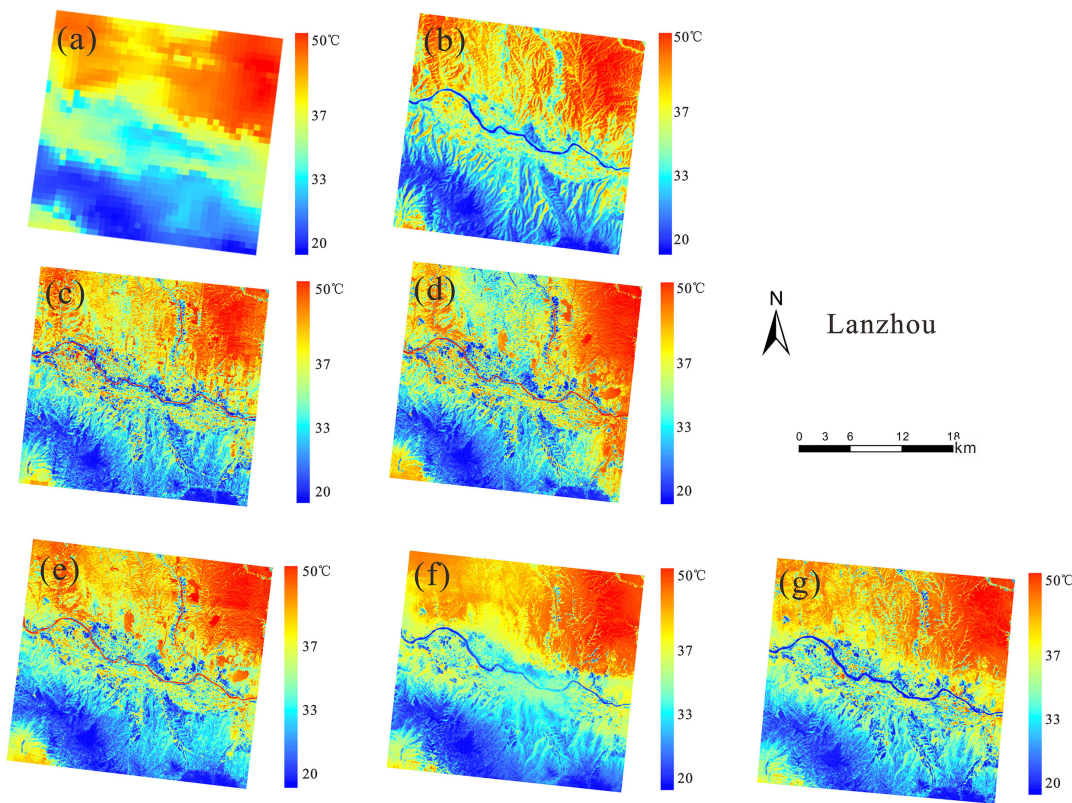


Fig. 9. Spatial distribution of LSTs in Lanzhou. (a) MODIS LST (1000 m). (b) Landsat 8 LST (100 m). (c) TsHARP downscaled LST (100 m). (d) GWR_VD downscaled LST (100 m). (e) GWAR_VD downscaled LST (100 m). (f) GWR_BD downscaled LST (100 m). (g) GWAR_BD downscaled LST (100 m).

TABLE VI
DOWNSCALING STATISTICS OF RMSE AND MAE BETWEEN LANDSAT 8 LST AND DOWNSCALED LSTs IN BEIJING

| Model | RMSE (℃) | MAE (℃) |
|---|---|---|
| GWAR_BD | 1.37 | 0.86 |
| GWR_BD | 2.01 | 1.66 |
| GWAR_VD | 1.92 | 1.45 |
| GWR_VD | 2.20 | 1.73 |
| TsHARP | 2.53 | 2.04 |

TABLE VII
DOWNSCALING STATISTICS OF RMSE AND MAE BETWEEN LANDSAT 8 LST AND DOWNSCALED LSTs IN LANZHOU

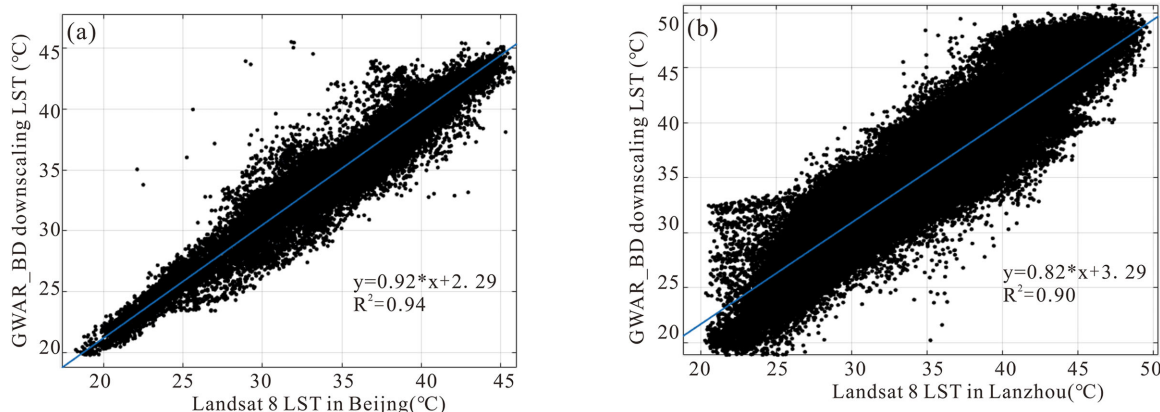| Model | RMSE (℃) | MAE (℃) |
|---|---|---|
| GWAR_BD | 1.76 | 1.33 |
| GWR_BD | 2.34 | 2.13 |
| GWAR_VD | 2.15 | 1.84 |
| GWR_VD | 3.02 | 2.65 |
| TsHARP | 3.46 | 2.94 |



Fig. 10. Scatterplots and regression relationship between downscaled LSTs from the GWAR-based and Landsat 8 LST at a 100-m spatial resolution (a) in Beijing and (b) in Lanzhou.

In these two areas, both the RMSE and the MAE of the GWAR_BD-based algorithm are the lowest [RMSE: 1.37 ℃ (Beijing) and 1.76 ℃ (Lanzhou), MAE: 0.86 ℃ (Beijing), and 1.33 ℃ (Lanzhou)]. The RMSE and MAE of the TsHARP-based algorithm are the highest [RMSE: 2.53 ℃ (Beijing) and 3.46 ℃ (Lanzhou), MAE: 2.04 ℃ (Beijing), and 2.94 ℃ (Lanzhou)]. The RMSE and MAE of the GWAR_BD-based algorithm are lower than those of the TsHARP algorithm and that of the GWR_VD algorithm and the GWAR_VD-based algorithm are also lower than the GWR_BD-based algorithm. These results indicate that with the same explanatory variables, the GWAR-based algorithm is better than the GWR-based algorithm. The RMSE and MAE of the GWAR_BD-based algorithm are lower

than those of the GWAR_VD-based algorithm, and that of GWR_BD-based algorithm are also lower than the GWR_VD-based algorithm. Therefore, when the algorithm is the same, the explanatory variable combination of DEM and NDBI has better downscaled results than the DEM and NDVI. Therefore, the GWAR-based algorithm with the explanatory variables of DEM and NDBI is more effective for LST downscaling in the study areas.

Fig. 10(a) and (b) displays the scatterplot and regression relationship comparison of the downscaled LSTs and Landsat 8 LST derived from GWAR-based algorithm, and the explanatory variables are DEM and NDBI in the two study areas, Beijing and Lanzhou, respectively. The relationship between the Landsat 8

LST and downscaled LSTs can be represented clearly by the scatterplot.

Fig. 10 shows scatterplots of the downscaled LST based on the GWAR_BD algorithm and Landsat 8 LST in the two study areas with a spatial resolution of 100 m. Fig. 10 indicates that the scatter had a distribution closer to the 1:1 line and that the $R^2$ of Beijing and Lanzhou is 0.94 and 0.90, respectively, which indicates that the proposed GWAR_BD-based algorithm achieved the better result. Fig. 10 shows that the downscaled LSTs based on the GWAR_BD algorithm are satisfactory in the study areas.

## V. CONCLUSION

LST is an important environmental variable, and LST data at higher spatial resolution are favorable for research on environmental problems. In this article, we proposed a new LST downscaling algorithm that uses the GWAR model to downscale the spatial resolution of MODIS LST from 1000 to 100 m. We chose DEM and NDBI as the explanatory variables to downscale the LST and the TsHARP-based and GWR-based algorithms as the comparison algorithms. In this article, Landsat 8 is the reference LST used to verify the downscaled LST.

In this study, comparing the DEM and NDBI with the DEM and NDVI as the explanatory variables, the downscaled results indicated that the explanatory variable combination of DEM and NDBI achieves better downscaled results than that of DEM and NDVI. This result occurs because the relationship between LST and NDVI is not a linear relationship in the mixed with water, bare soil, and other land cover types. A larger error in soil moisture content occurs when the DEM and NDVI are used as the explanatory variables. In addition, the downscaled result of the TsHARP algorithm contains boxy artifacts, and the result of GWR-based algorithm has a smoothing effect. Calculating the statistics of the RMSE and MAE between the Landsat 8 LST and downscaled LSTs, the GWAR-based algorithm achieved the lowest RMSE (1.35 °C in Beijing and 1.76 °C in Lanzhou) and MAE (0.86 °C in Beijing and 1.33 °C in Lanzhou). Comparing the Landsat 8 LST with the downscaled LSTs at a 100-m spatial resolution, the $R^2$ values of the GWAR-based algorithm in the study areas are 0.94 (Beijing) and 0.90 (Lanzhou). The GWAR-based algorithm considers both the spatial nonstationary and the spatial autocorrelation. Therefore, the downscaled results of the GWAR-based algorithm with DEM and NDBI as the explanatory variables can capture additional spatial details and achieve better downscaled results than the other methods.

Although the GWAR-based algorithm achieved better results than the other algorithms, several problems require further investigation. First, the GWAR-based algorithm with DEM and NDBI as the explanatory variables only considers the spatial features of the LST, but the temporal variability is ignored. Second, the spatial autocorrelation differs in different land cover types, and, therefore, we could investigate the spatial autocorrelation based on land cover types in the future. Third, we should add different areas and time images to investigate the downscaling methods. In addition, we could attempt to use other high spatial resolution data to verify the applicability of this algorithm for other data. Therefore, an in-depth study will be conducted in the future.

In this article, we proposed the GWAR-based algorithm for LST downscaling, an approach that considers the spatial nonstationary and spatial autocorrelation simultaneously in the study of spatial variables, and we chose the DEM and NDBI as the explanatory variables in the downscaling process. In short, this article offers a new method for the study of LST downscaling and improves the results of LST downscaling, which are essential for the future study of LST.

## REFERENCES

[1] Z.-L. Li *et al.*, "Satellite-derived land surface temperature: Current status and perspectives," *Remote Sens. Environ.*, vol. 131, no. 131, pp. 14–37, 2013.

[2] Y. Jiang and Q. Weng, "Estimation of hourly and daily evapotranspiration and soil moisture using downscaled LST over various urban surfaces," *GISci. Remote Sens.*, vol. 54, no. 1, pp. 95–117, 2017.

[3] W. Su, G. Yang, S. Chen, and Y. Yang, "Measuring the pattern of high temperature areas in urban greenery of Nanjing city, China," *Int. J. Environ. Res. Public Health*, vol. 9, no. 8, pp. 2922–2935, 2012.

[4] K. Zakšek and K. Oštir, "Downscaling land surface temperature for urban heat island diurnal cycle analysis," *Remote Sens. Environ.*, vol. 117, pp. 114–124, 2012.

[5] O. Merlin *et al.*, "Disaggregation of MODIS surface temperature over an agricultural area using a time series of Formosat-2 images," *Remote Sens. Environ.*, vol. 114, no. 11, pp. 2500–2512, 2010.

[6] P. Wu, H. Shen, L. Zhang, and F. M. Göttsche, "Integrated fusion of multi-scale polar-orbiting and geostationary satellite observations for the mapping of high spatial and temporal resolution land surface temperature," *Remote Sens. Environ.*, vol. 156, pp. 169–181, 2015.

[7] Q. Weng, D. Lu, and J. Schubring, "Estimation of land surface temperature–vegetation abundance relationship for urban heat island studies," *Remote Sens. Environ.*, vol. 89, no. 4, pp. 467–483, 2004.

[8] J. Luo *et al.*, "Applying remote sensing techniques to monitoring seasonal and interannual changes of aquatic vegetation in Taihu Lake, China," *Ecol. Indicators*, vol. 60, pp. 503–513, 2016.

[9] Y. Mo, B. Momen, and M. Kearney, "Quantifying moderate resolution remote sensing phenology of Louisiana coastal marshes," *Ecol. Model.*, vol. 312, pp. 191–199, 2015.

[10] J. I. Fisher and J. F. Mustard, "Cross-scalar satellite phenology from ground, Landsat, and MODIS data," *Remote Sens. Environ.*, vol. 109, no. 3, pp. 261–273, 2007.

[11] M. Wu *et al.*, "Reconstruction of daily 30 m data from HJ CCD, GF-1 WFV, Landsat, and MODIS data for crop monitoring," *Remote Sens.*, vol. 7, no. 12, pp. 16293–16314, 2015.

[12] Q. Weng and F. Peng, "Modeling diurnal land temperature cycles over Los Angeles using downscaled GOES imagery," *ISPRS J. Photogramm. Remote Sens.*, vol. 97, pp. 78–88, 2014.

[13] S. Kandasamy and R. Fernandes, "An approach for evaluating the impact of gaps and measurement errors on satellite land surface phenology algorithms: Application to 20 year NOAA AVHRR data over Canada," *Remote Sens. Environ.*, vol. 164, pp. 114–129, 2015.

[14] C. J. Tomlinson, L. Chapman, J. E. Thornes, and C. Baker, "Remote sensing land surface temperature for meteorology and climatology: A review," *Meteorol. Appl.*, vol. 18, no. 3, pp. 296–306, 2011.

[15] J. Verbesselt, R. Hyndman, A. Zeileis, and D. Culvenor, "Phenological change detection while accounting for abrupt and gradual trends in satellite image time series," *Remote Sens. Environ.*, vol. 114, no. 12, pp. 2970–2980, 2010.

[16] W. Zhan *et al.*, "Disaggregation of remotely sensed land surface temperature: Literature survey, taxonomy, issues, and caveats," *Remote Sens. Environ.*, vol. 131, no. 8, pp. 119–139, 2013.

[17] E. Pardo-Igúzquiza, M. Chica-Olmo, and P. Atkinson, "Downscaling cokriging for image sharpening," *Remote Sens. Environ.*, vol. 102, no. 1, pp. 86–98, 2006.

[18] D. Liu and R. Pu, "Downscaling thermal infrared radiance for subpixel land surface temperature retrieval," *Sensors*, vol. 8, no. 4, pp. 2695–2706, 2008.

[19] S. Liang, *Quantitative Remote Sensing of Land Surfaces*. Hoboken, NJ, USA: Wiley, 2005.

[20] M. Wu *et al.*, "An improved high spatial and temporal data fusion approach for combining Landsat and MODIS data to generate daily synthetic Landsat imagery," *Inf. Fusion*, vol. 31, pp. 14–25, 2016.

[21] F. Gao, J. G. Masek, M. R. Schwaller, and F. Hall, "On the blending of the Landsat and MODIS surface reflectance: predicting daily Landsat surface reflectance," *IEEE Trans. Geosci. Remote Sens.*, vol. 44, no. 8, pp. 2207–2218, Aug. 2006.

[22] Q. Weng, P. Fu, and F. Gao, "Generating daily land surface temperature at Landsat resolution by fusing Landsat and MODIS data," *Remote Sens. Environ.*, vol. 145, no. 8, pp. 55–67, 2014.

[23] W. Mingquan, H. Wenjiang, N. Zheng, W. Changyao, L. Wang, and Y. Bo, "Validation of synthetic daily Landsat NDVI time series data generated by the improved spatial and temporal data fusion approach," *Inf. Fusion* vol. 40, pp. 34–44, 2018.

[24] O. Duran and M. Petrou, "Subpixel temporal spectral imaging," *Pattern Recognit. Lett.*, vol. 48, no. 1, pp. 15–23, 2014.

[25] F. Maselli, M. A. Gilabert, and C. Conese, "Integration of high and low resolution NDVI data for monitoring vegetation in Mediterranean environments," *Remote Sens. Environ.*, vol. 63, no. 3, pp. 208–218, 1998.

[26] B. Zhukov, D. Oertel, F. Lanzl, and G. Reinhackel, "Unmixing-based multisensor multiresolution image fusion," *IEEE Trans. Geosci. Remote Sens.*, vol. 37, no. 3, pp. 1212–1226, May 1999.

[27] F. Maselli, "Definition of spatially variable spectral endmembers by locally calibrated multivariate regression analyses," *Remote Sens. Environ.*, vol. 75, no. 1, pp. 29–38, 2001.

[28] W. Zhan, Y. Chen, J. Zhou, J. Li, and W. Liu, "Sharpening thermal imageries: A generalized theoretical framework from an assimilation perspective," *IEEE Trans. Geosci. Remote Sens.*, vol. 49, no. 2, pp. 773–789, Feb. 2011.

[29] W. P. Kustas, J. M. Norman, M. C. Anderson, and A. French, "Estimating subpixel surface temperatures and energy fluxes from the vegetation index–radiometric temperature relationship," *Remote Sens. Environ.*, vol. 85, no. 4, pp. 429–440, 2003.

[30] N. Agam, W. P. Kustas, M. C. Anderson, F. Li, and C. Neale, "A vegetation index based technique for spatial sharpening of thermal imagery," *Remote Sens. Environ.*, vol. 107, no. 4, pp. 545–558, 2007

[31] N. Agam, W. P. Kustas, M. C. Anderson, F. Li, and P. Colaizzi, "Utility of thermal image sharpening for monitoring field-scale evapotranspiration over rainfed and irrigated agricultural regions," *Geophys. Res. Lett.*, vol. 35, no. 2, pp. 196–199, 2008.

[32] J. Qiu, J. Yang, Y. Wang, and S. Hua, "A comparison of NDVI and EVI in the DisTrad model for thermal sub-pixel mapping in densely vegetated areas: A case study in Southern China," *Int. J. Remote Sens.*, vol. 39, no. 8, pp. 2105–2118, 2018.

[33] X. Pan, X. Zhu, Y. Yang, C. Cao, X. Zhang, and L. Shan, "Applicability of downscaling land surface temperature by using normalized difference sand index," *Sci. Rep.*, vol. 8, no. 1, 2018, Art. no. 9530.

[34] V. M. Bindhu, B. Narasimhan, and K. P. Sudheer, "Development and verification of a non-linear disaggregation method (NL-DisTrad) to downscale MODIS land surface temperature to the spatial scale of Landsat thermal data to estimate evapotranspiration," *Remote Sens. Environ.*, vol. 135, no. 8, pp. 118–129, 2013.

[35] C. Hutengs and M. Vohland, "Downscaling land surface temperatures at regional scales with random forest regression," *Remote Sens. Environ.*, vol. 178, no. 2, pp. 127–141, 2016.

[36] Y. Yang, C. Cao, X. Pan, X. Li, and X. Zhu, "Downscaling land surface temperature in an arid area by using multiple remote sensing indices with random forest regression," *Remote Sens.*, vol. 9, no. 8, 2017, Art. no. 789.

[37] Z. Ji, S. Liu, M. Li, W. Zhan, Z. Xu, and T. Xu, "Quantification of the scale effect in downscaling remotely sensed land surface temperature," *Remote Sens.*, vol. 8, 2016, Art. no. 975.

[38] X. Chen, W. Li, J. Chen, W. Zhan, and Y. Rao, "A simple error estimation method for linear-regression-based thermal sharpening techniques with

the consideration of scale difference," *Geo-spatial Inf. Sci.*, vol. 17, no. 1, pp. 54–59, 2014.

[39] S. B. Duan and Z. Li, "Spatial downscaling of MODIS land surface temperatures using geographically weighted regression: Case study in Northern China," *IEEE Trans. Geosci. Remote Sci.*, vol. 54, no. 11, pp. 6458–6469, Nov. 2016.

[40] O. Pereira, A. Melfi, C. Montes, and Y. Lucas, "Downscaling of ASTER thermal images based in geographically weighted regression kriging," *Remote Sens*, vol. 10, 2018, Art. no. 633.

[41] Y. Peng, W. Li, X. Luo, and H. Li, "A geographically and temporally weighted regression model for spatial downscaling of MODIS land surface temperatures over urban heterogeneous regions," *IEEE Trans. Geosci. Remote Sens.*, vol. 57, no. 7, pp. 5012–5027, Jul. 2019

[42] A. Sekertekin, S. H. Kutoglu, and S. Kaya, "Evaluation of spatio-temporal variability in land surface temperature: A case study of Zonguldak, Turkey," *Environ. Monit. Assess*, vol. 188, no. 1, pp. 1–15, 2016.

[43] F. Wang, Z. Qin, C. Song, L. Tu, A. Karnieli, and S. Zhao, "An improved mono-window algorithm for land surface temperature retrieval from Landsat 8 thermal infrared sensor data," *Remote Sens.*, vol. 7, no 4, pp. 4268–4289, 2015

[44] Z. Qin, A. Karnieli, and P. Berliner, "A mono-window algorithm for retrieving land surface temperature from Landsat TM data and its application to the Israel–Egypt border region," *Int. J. Remote Sens.*, vol. 22, no. 18, pp. 3719–3746, 2001.

[45] M. I. Ndossi and U. Avdan, "Application of open source coding technologies in the production of land surface temperature (LST) maps from Landsat: A PyQGIS plugin," *Remote Sens.*, vol. 8, no. 5, 2016, Art. no. 413.

[46] F. B. Balcik and E. M. Ergene, "Determining the impacts of land cover/use categories on land surface temperature using Landsat8-OLI," *Int. Arch. Photogramm., Remote Sens. Spatial Inf. Sci.*, vol XLI-B8, pp. 251–256, 2016, doi: 10.5194/isprsarchives-XLI-B8-251-2016.

[47] J.-C. Jimenez-Munoz and J. A. Sobrino, "Split-window coefficients for land surface temperature retrieval from low-resolution thermal infrared sensors," *IEEE Geosci. Remote Sens.*, vol. 5, no. 4, pp. 806–809, Oct. 2008.

[48] T. Li and Q. Meng, "A mixture emissivity analysis method for urban land surface temperature retrieval from Landsat 8 data," *Landscape Urban Plan.*, vol. 179, pp. 63–71, 2018

[49] L. Vlassova, F. Perez-Cabello, H. Nieto, P. Martín, D. Riaño, and J. Riva, "Assessment of methods for land surface temperature retrieval from Landsat-5 TM images applicable to multiscale tree-grass ecosystem modeling," *Remote Sens.*, vol. 6, no. 5, pp. 4345–4368, 2014.

[50] K. Tan, Z. Liao, P. Du, and L. Wu, "Land surface temperature retrieval from Landsat 8 data and validation with geosensor network," *Front. Earth Sci.*, vol. 11, no. 1, pp. 20–34, 2017.

[51] Z. Wan and J. Dozier, "A generalized split-window algorithm for retrieving land-surface temperature from space," *IEEE Trans. Geosci. Remote Sens.*, vol. 34, no. 4, pp. 892–905, Jul. 1996.

[52] S. B. Duan *et al.*, "Radiance-based validation of land surface temperature products derived from Collection 6 MODIS thermal infrared data," *Int. J. Appl. Earth Obs. Geoinf.*, vol. 70, pp. 84–92, 2018.

[53] S. B. Duan, Z. L. Li, and J. Cheng, "Cross-satellite comparison of operational land surface temperature products derived from MODIS and ASTER data over bare soil surfaces," *ISPRS J Photogramm. Remote Sens.*, vol. 126, pp. 1–10, 2017.

[54] D. Mcmillen, "Geographically weighted regression: The analysis of spatially varying relationships," *Amer. J. Agric. Econ.*, vol. 86, no. 2, pp. 554–556, 2004.

[55] B. Wu, R. Li, and B. Huang, "A geographically and temporally weighted autoregressive model with application to housing prices," *Int. J. Geogr. Inf. Sci.*, vol. 28, no. 5, pp. 1186–1204, 2014.

[56] J. P. Lesage, "The theory and practice of spatial enconometrics," Dept. Econ., Univ. Toledo, Toledo, OH, USA, 1999.

[57] Calvo, Ernesto, and M. Escolar, "A geographically weighted approach to ecological inference," *American J. Political Sci.*, vol. 47, no. 1, pp. 188–209, 2002.

[58] T. Hengl, G. B. M. Heuvelink, M. P. Tadić, and E. Pebesma, "Spatio-temporal prediction of daily temperatures using time-series of MODIS LST images," *Theor. Appl. Climatol.*, vol. 107, no. 1/2, pp. 265–277, 2012.

[59] G. Yang, R. Pu, C. Zhao, W. Huang, and J. Wang, "Estimation of subpixel land surface temperature using an endmember index based technique: A case examination on ASTER and MODIS temperature products over a heterogeneous area," *Remote Sens. Environ.*, vol. 115, no. 5, pp. 1202–1219, 2011.

[60] H. Li and Q. Liu, "Comparison of NDBI and NDVI as indicators of surface urban heat island effect in MODIS imagery," *Proc. SPIE*, vol. 7285, 2008, Art. no. 728503.

[61] L. Habin, W. Zhengquan, and W. Qingcheng, "Theory and methodology of spatial heterogeneity quantification," *J. Appl. Ecol.*, vol. 9, pp. 651–657, 1998.

[62] H. Govil, S. Guha, A. Dey, and N. Gill, "Seasonal evaluation of downscaled land surface temperature: A case study in a humid tropical city," *Heliyon*, vol. 5, 2019, Art. no. e01923.

[63] H. J. Yang, Z. T. Cong, Z. W. Liu, and Z. Lei, "Estimating sub-pixel temperatures using the triangle algorithm," *Int. J. Remote Sens.*, vol. 31, no. 23, pp. 6047–6060, 2010.

[64] Z. Wan, "New refinements and validation of the collection-6 MODIS land-surface temperature/emissivity product," *Remote Sens. Environ.*, vol. 140, pp. 36–45, Jan. 2014.

[65] D. Mutiibwa, S. Strachan, and T. Albright, "Land surface temperature and surface air temperature in complex terrain," *IEEE J. Sel. Topics Appl. Earth Observ. Remote Sens.*, vol. 8, no. 10, pp. 1–13, Oct. 2015.

[66] G. Simó *et al.*, "Landsat and local land surface temperatures in a heterogeneous terrain compared to MODIS values," *Remote Sens.*, vol. 8, no. 10, 2016, Art. no. 849.

[67] X. M. Zhu, X. H. Wang, D. J. Yan, Z. Liu, and Y. Zhou, "Analysis of remotely-sensed ecological indexes' influence on urban thermal environment dynamic using an integrated ecological index: A case study of Xi'an, China," *Int. J. Remote Sens.*, vol. 40, no. 9, pp. 3421–3447, 2019.

[68] N. Agam, W. P. Kustas, M. C. Anderson, F. Li, and P. Colaizzi, "Utility of thermal sharpening over Texas high plains irrigated agricultural fields," *J. Geophys. Res., Atmos.*, vol. 112, 2007, Art. no D19110.

[69] S. Xu, C. Wu, L. Wang, A. Gonsamo, Y. Shen, and Z. Niu, "A new satellite-based monthly precipitation downscaling algorithm with non-stationary relationship between precipitation and land surface characteristics," *Remote Sens. Environ.*, vol. 162, pp. 119–140, 2015.

**Shumin Wang** was born in Shandong, China, in 1994. She is currently working toward the M.S. degree in remote sensing image processing from the Chongqing University of Posts and Telecommunications, Chongqing, China.

Her research interests include urban thermal infrared remote sensing, remote sensing image processing, and ecological environment monitoring and evaluating.

**Xiaobo Luo** received the B.S. degree in geographic information system (GIS) from the Institute of Geophysics and Geomatics, China University of Geosciences, Wuhan, China, in 1999, the M.S. degree in GIS from the School of Information Engineering, Chinese Academy of Sciences, Wuhan, China, in 2004, and the Ph.D. degree in cartography and GIS from the Institute of Remote Sensing Applications, Chinese Academy of Sciences, Beijing, China, in 2010.

He is currently a Professor with the Chongqing University of Posts and Telecommunications, Chongqing, China. His research interests include urban thermal infrared remote sensing, remote sensing image processing, and ecological environment monitoring and evaluation.

**Yidong Peng** (Student Member, IEEE) was born in Chongqing, China, in 1988. He received the M.S. degree in remote sensing image processing from the Chongqing University of Posts and Telecommunications, Chongqing, China, in 2017, where he is currently working toward the Ph.D. degree in computer science and technology with the Chongqing Key Laboratory of Image Cognition.

His research interests include urban thermal infrared remote sensing, remote sensing image processing, and ecological environment monitoring and evaluating.